# Closed-Edged Graphene Nanoribbons from Large-Diameter Collapsed Nanotubes

**Chenguang Zhang,[†,⊥] Ksenia Bets,[‡] Seung Soo Lee,[†] Zhengzong Sun,[†] Francesca Mirri,[§] Vicki L. Colvin,[†] Boris I. Yakobson,[†,‡] James M. Tour,[†,‡,*] and Robert H. Hauge[†,*]**

[†]Department of Chemistry and Richard E. Smalley Institute for Nanoscale Science and Technology, [‡]Department of Mechanical Engineering and Materials Science, and [§]Department of Chemical and Biomolecular Engineering, Rice University, 6100 Main Street, Houston, Texas 77005, United States and [⊥]School of Materials Science and Engineering, Tianjin University, No. 92 Weijin Road, Tianjin, China 300072

**ABSTRACT** The diameter dependence of the collapse of single- and double-walled carbon nanotubes to two- and four-walled graphene nanoribbons with closed edges ($CE_xGNRs$) has been experimentally determined and compared to theory. TEM and AFM were used to characterize nanotubes grown from preformed 4.0 nm diameter aluminum–iron oxide particles. Experimental data indicate that the energy equivalence point (the diameter at which the energy of a round and fully collapsed nanotube is the same) is 2.6 and 4.0 nm for single- and double-walled carbon nanotubes, respectively. Molecular dynamics simulations predict similar energy equivalence diameters with the use of $\varepsilon = 54$ meV/pair to calculate the carbon–carbon van der Waals interaction.

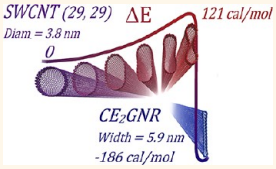


**KEYWORDS:** collapsed nanotube · graphene nanoribbon · single-walled carbon nanotubes · double-walled carbon nanotubes · aluminum–iron oxide nanoparticles · molecular dynamics simulation · carbon–carbon van der Waals interaction

Carbon nanotubes (CNTs) with different diameters and helicity have distinct chemical and physical properties. Diameter-selective and diameter-controlled growth of CNTs has been developed for specific applications, such as field-effect transistors,[1] field-emission displays,[2] and hydrogen storage.[3] Synthesis of large-diameter CNTs, especially single-walled carbon nanotubes (SWCNTs) within a range of 1.4–5.6 nm, has been realized with laser vaporization,[4] arc discharge,[5] and chemical vapor deposition (CVD) method.[6–8]

When the diameter increases, cylindrical SWCNTs become energetically unstable. A number of theoretical studies[9–18] have demonstrated that there exists a tube diameter ($D_{eqe}$) where the energy of the collapsed tube is the same as that of the round geometry. Near the $D_{eqe}$ energy, there exists a diameter region where both geometries can coexist at high temperatures. This has been referred to as a metastable region for the CNT structure. The cross section configuration of the fully collapsed structure is composed of two highly strained circular edges bridged by a flat middle section. We refer to this geometry as a closed-edged graphene nanoribbon ($CE_xGNR$) configuration, which is stabilized by van der Waals interaction between two opposing walls. Theoretical studies have found $D_{eqe}$ to be an increasing function of the number of walls.[9,10] Table 1 summarizes a number of reported values of $D_{eqe}$ from the literature and the methodologies employed to deduce them. In those studies, $D_{metastable}$ ranges were given for SWCNT[14–16] and double-walled carbon nanotubes (DWCNTs);[17,18] $D_{metastable}$ ranges and $D_{eqe}$ for triple-walled carbon nanotubes (TWCNTs) have also been calculated.[18]

In addition to the diameter,[10,13,14,18] SWCNT collapse is also correlated to external factors, such as temperature,[19] pressure,[20–22] van der Waals force induced by a substrate[23] or neighboring tubes in bundles,[13,24] toxic addition in the reaction system,[25] mechanical strain,[26,27] and electron bombardment.[28] Modeling of the transition between a cylindrical and collapsed configuration in different environments has been studied extensively.[19,29–31] Furthermore, unusual edge states[32] and promising electronic,[33–35] mechanical,[29] and electromechanical behavior[30] of collapsed SWCNTs have been documented and predicted. Nanotube collapsing allows for the band gap modification by its transverse self-collapse, avoiding the employment of structural perturbations which disturb the $sp^2$ bonding framework or the position of the tube ends.[34]

Although the formation of a collapsed structure is largely independent of tube

* Address correspondence to tour@rice.edu, hauge@rice.edu.

Received for review March 8, 2012 and accepted June 7, 2012.

**Published online June 07, 2012**
**10.1021/nn301039v**

**TABLE 1. Summary of Values of Equivalent Energy Points for SWCNTs and DWCNTs in the Literature and the Methodologies Employed**

| ref | $D_{eqe}$ for SWCNT (nm) | $D_{eqe}$ for DWCNT (nm) | methodology |
|---|---|---|---|
| 10 | 3.6—8.6 | 3.8—10.4 | experimental and continuum model analysis (bending modulus used $k = 1.4$ eV; $\varepsilon_{vdW} = 25$—100 meV/atom; crossover shapes were calculated from geometrical assumptions) |
| 11 | 5.9—6.0 | | molecular dynamics simulation using MPSim (force field, derived through QM calculations; bending modulus $k = 912$—963 GPa depending on chirality) |
| 12 | 2 | | molecular dynamics simulation (REBO potential to represent covalent bonds; adaptive Lennard-Jones potential to represent van der Waals interaction) |
| 13 | 2.2 | | extrapolation from molecular dynamics simulations of collapsing of hexagonally close-packed bundles of SWNT using DL_POLY code (macromolecular force field DREIDING parametrized for carbon) |
| 15 | 4.1 | 5.0 | atomic-scale finite-element method simulation and order-$N$ atomistic simulation method based on Brenner potential for carbon ($\varepsilon_{vdW} = 2.39$ meV/atom) |
| 16 | 1.9 | | continuum model analysis and molecular simulation using Discover molecular dynamics program through Materials Studio 3.0 (polymer consistent force field used) |
| 17 | 6.2 | 8.0 | atomistic simulations (second-generation Tersoff—Brenner potential and Lennard-Jones potential; $\varepsilon_{vdW} = 2.39$ meV/atom) |
| present work | 2.6 | 4.0 | molecular dynamics simulation using LAMMPS (AIREBO potential with no torsion term; $\varepsilon_{vdW} = 53.6$ meV/pair) |

chirality,[13,17] the structure of collapsed SWCNTs can be flat, warped, or twisted[14,36] due to lattice registry dependent van der Waals interaction between the two opposing walls. The morphology of collapsed nanotubes has been demonstrated by TEM,[9,37,38] STM,[35] and AFM[39,40] measurements. In previous efforts in synthesizing large-diameter CNTs, the Zettl group,[9] Kiang *et al.*,[41] and the Ajayan group[42] have observed the collapsed and twisted structures of multiwalled carbon nanotubes (MWCNTs), SWCNTs, and DWCNTs, respectively. Recently, Alvarez *et al.*[43] observed collapsed DWCNTs with a ribbon-like structure. However, very few observations were obtained in TEM images, and the collapsed phenomenon of few-walled CNTs was not discussed in detail. In this study, synthesis of large-diameter few-walled CNTs was accomplished using nearly monodisperse aluminum ferrite nanoparticles (Figure 1). TEM characterization was used to distinguish between uncollapsed and collapsed carbon nanotubes based on whether tubes exhibited kinks as expected for collapsed tubes but not for uncollapsed tubes. Formulas for conversion of the widths of collapsed tubes to their respective round configurations were theoretically determined and permitted a direct comparison of diameter distributions for both collapsed and uncollapsed tubes.

## RESULTS AND DISCUSSION

Figure 1b displays a TEM image of 4.0 nm preformed $AlFe_2O_4$ nanoparticles. These nanoparticles have a narrow size distribution, with an average diameter of $4.0 \pm 0.4$ nm (inset in Figure 1b). The size homogeneity of the preformed nanoparticles and their chemical composition were also demonstrated with lower magnification TEM image, AFM image, and X-ray diffraction (XRD) pattern in Figure S1 (Supporting Information).

The nearly monodispersed nanoparticles have been employed in the synthesis of large-diameter CNTs in previous studies.[7,43] It has been shown that by using these well-defined preformed nanoparticles, one is able to achieve diameter-controlled synthesis of CNTs. An additional advantage is that particle size can be controlled over a large size range. This cannot be achieved by catalyst evaporation onto a substrate to form catalyst islands. The dense and vertical growth of nanotube carpet on the $Al_2O_3/SiO_2$ substrate was achieved in a CVD process from $AlFe_2O_4$ nanoparticles with various concentrations (from 22 to 375 nM, as shown in Figure S2). As can be seen in the SEM image (Figure 1c), a carpet height of $\sim$100 $\mu$m was obtained in 10 min growth from the nanoparticles with an optimized concentration (25 nM), indicating a high growth rate of $\sim$10 $\mu$m/min. A portion indicated by a square frame in Figure 1c is shown in a higher magnification SEM image (Figure 1d). A large amount of kinking and bending is evident. The TEM picture (Figure 1e) shows that the sample is predominantly SWCNTs, with typically bent and twisted structures, indicating large numbers of collapsed SWCNTs. Catalyst particles encapsulated at the nanotube ends are also visible. Figure 1f shows a Raman spectra of the nanotube sample, which was taken from both the top and

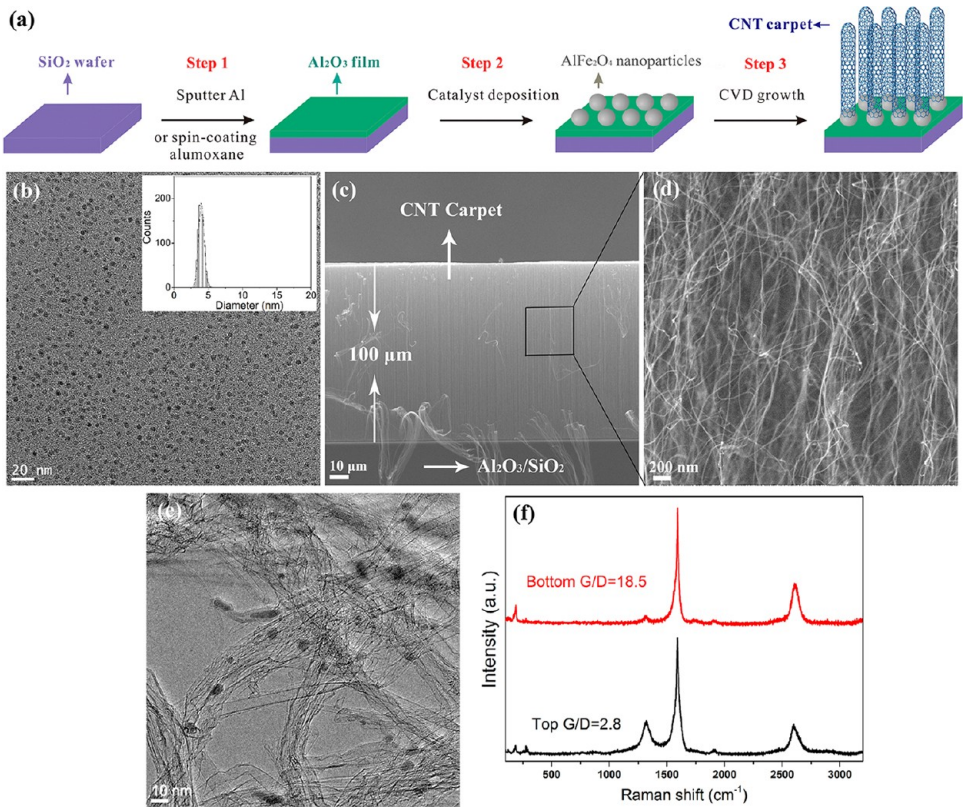


**Figure 1. Synthesis of a large-diameter CNT carpet from monodispersed $AlFe_2O_4$ preformed nanoparticles. (a) Schematic description of the preparation process of the collapsed CNTs. (Step 1) Sputtering aluminum or spin coating water-soluble alumina particles on the $SiO_2$ surface to fabricate the $Al_2O_3/SiO_2$ substrate. (Step 2) Drop drying preformed $AlFe_2O_4$ nanoparticle solution on the substrate surface and calcining at 200 °C to form a metal oxide catalyst layer. (Step 3) Growing the CNT carpets by water-assisted CVD method. (b) TEM image of uniformly dispersed performed nanoparticles with oleic acid coating. The inset histogram shows the diameter distribution of the preformed nanoparticle, with an average size of $4.0 \pm 0.4$ nm. (c) SEM image of the CNT carpet with a height of ~100 $\mu$m grown on the $Al_2O_3/SiO_2$ substrate in 10 min growth. (d) Close-up SEM image of the CNT arrays at higher magnification, corresponding to the indicated region in (c). (e) TEM image of the large-diameter CNT. (f) Raman spectra of the top and bottom region of the CNT carpet, showing G/D ratios of 2.8 and 18.5, respectively.**

bottom region of the nanotube carpet using a wavelength of 633 nm for excitation. Radial breathing modes (RBMs) are clearly observed in the range of 100−300 $cm^{-1}$. Moreover, the subsidiary peak shown in the low-frequency range of the G band and the lack of subsidiary peak on its high wavenumber side indicate that the nanotubes in the sample are mainly single-walled,[38] in agreement with the TEM observation (Figure 1e). The carpet bottom shows a G/D ratio of ~18.5, much higher than that in the top region (~2.8). It is found that the base-growth mechanism[44] dominates in our conditions since residues of catalyst particles in high density can still be seen anchored to the substrate after removing the nanotubes. Catalytic processes that cause amorphous carbon formation during the initial stage of nanotube growth are likely responsible for the lower G/D ratio commonly found at the top of a carpet. The bottom G/D ratio is a better indicator of nanotube quality, and we take the ratio of 16−18:1 to be an indicator of largely defect-free SWCNTs. Thus we expect their mechanical behavior to be quite similar to that for the calculated mechanical behavior of structurally perfect SWCNTs. We cannot exclude the possibility of twists or kinks of the nanotubes on the surface; however, there are large domains that appear free of those defects.

Figure 2 shows the TEM images of collapsed and uncollapsed nanotubes. Collapsed SWCNTs, DWCNTs, and TWCNTs are shown in Figure 2a−c. Kinked (Figure 2a), folded (Figure 2b), and twisted (Figure 2c) structures which are typical features of collapsed nanotubes[14] are clearly observed (as indicated by the arrows in Figure 2a−c). These structures are used as an identifier of closed-edged graphene nanoribbons. A collapsed and twisted MWCNT ribbon is also observed in Figure 2c. The widths of the flattened ribbons in this image formed by SWCNTs, DWCNTs, TWCNTs, and MWCNTs are found to be 4.6, 8.0, 7.8, and 8.2 nm, respectively. Previous studies have suggested that collapse does not necessarily occur throughout the entire tube[45] and is most likely caused by mechanical activation rather than thermal activation.[17] It has also been suggested that kinked deformations formed locally in some regions on the nanotube might serve

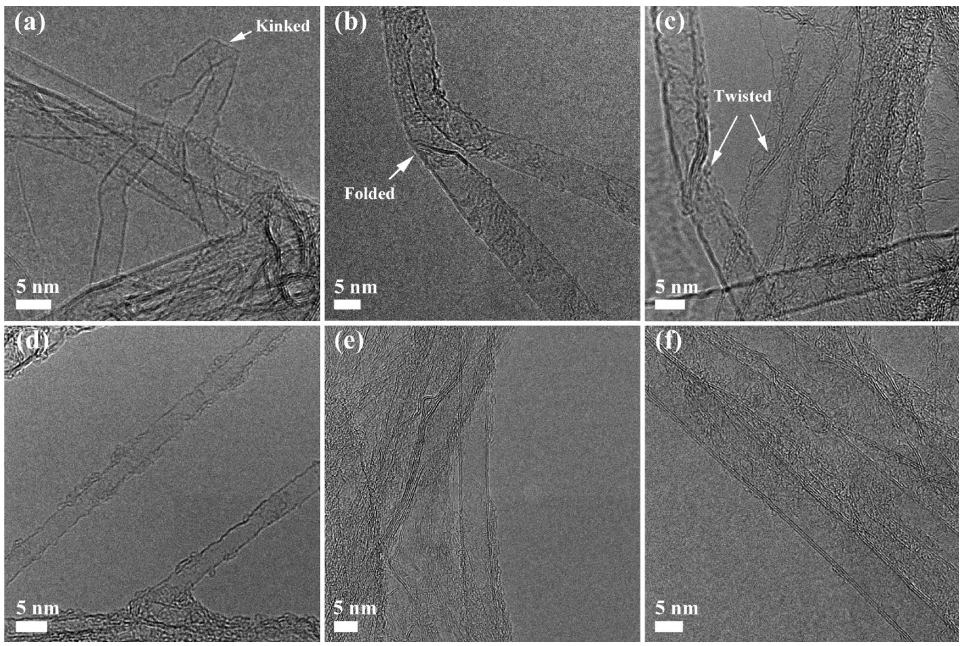


**Figure 2. TEM images of the collapsed and uncollapsed CNTs. TEM images for collapsed (a) SWCNTs, (b) DWCNTs, and (c) TWCNTs. TEM images for uncollapsed (d) SWCNTs, (e) DWCNTs, and (f) TWCNTs. Kinked, folded, and twisted deformation parts are shown in collapsed nanotubes, indicating they are collapsed to corresponding bilayer, four-layer, six-layer, and multilayer closed-edge graphene nanoribbons. The uncollapsed nanotubes are identified by their straight geometry, with typically smaller diameters than that of collapsed nanotubes.**

as an initiator for an entire flattening of a tube through a zipper effect.[9] Others have attributed collapsed structures to high pressure during the reaction.[46,47] Collapsed nanotubes with twisted structures have also been observed with multiwalled CNTs (MWCNTs) in other studies.[9,46] Lattice registration between opposing walls is thought to be responsible for the twisted phenomenon: the interaction between the two paralleled graphene walls (innermost walls in the DWCNTs, TWCNTs, and MWCNTs) tends to achieve the lowest energy AB stacking *via* the translations along radial and axial directions. Thus, achievement of more favorable interlayer registry acts as a driving force for twisting or warping of collapsed nanotubes. In order to better understand the difference of the structural characteristics between the collapsed and uncollapsed nanotubes in the TEM images, TEM pictures of the uncollapsed SWCNTs, DWCNTs, and TWCNTs are also provided in Figure 2d–f for comparison with the collapsed ones. We have assumed that the uncollapsed nanotubes are observed as straight structures without kinks and bends. The diameters of the uncollapsed SWCNTs, DWCNTs, and TWCNTs are observed to be 3.6, 6.3, and 7.1 nm, respectively, smaller than the observed widths of the collapsed nanotubes as expected. These structural and morphological features of the collapsed and uncollapsed nanotubes are utilized to distinguish these two counterparts during collection of their counts and performing the statistics detailed in the following discussion. More TEM pictures showing the collapsed nanotube features are provided in Figure S3.

The presence of the twisted collapsed nanotubes is usually observed to be free-standing, which suggests that the translations between the innermost two walls achieve a favorable lattice stacking which prevents the twisted ribbon from untwisting.[36] Tapping-mode AFM was used to study the collapsed structure of carbon nanotubes. A suspension of nanotubes was prepared by bath sonication in dichloroethane solution. Subsequently, a drop of the suspension was spin-coated onto the surface of a cleaned silicon wafer and dried at room temperature. The sample was analyzed by AFM (Digital Instruments, Nanoscope III Veeco Metrology Group, Santa Barbara, CA) using a TETRA 15/Au tip (K•TEK Nanotechnology LLC, Digital Instruments). The number of walls of a collapsed nanotube is defined from the height measurement information. It is known that the height of single graphene layer is around 0.34 nm, which is also the interlayer distance of graphite. Thus we infer that the heights of the fully collapsed SWCNTs (bilayer graphene), DWCNTs (four-layer graphene), TWCNTs (six-layer graphene), and four-walled nanotubes (eight-layer graphene) are around 0.7, 1.4, 2.0, and 2.7 nm, respectively, which we use for the following estimation of the number of walls for collapsed nanotubes. Our approximation is consistent with the definition for number of layers reported by Yu *et al.*[48] Shown in Figure 3a,c,e are AFM height images of a collapsed SWCNT, DWCNT, and TWCNT, respectively. Their corresponding height profiles are presented in Figure 3b,d,f. Images are shown in same height scale on each nanotube.

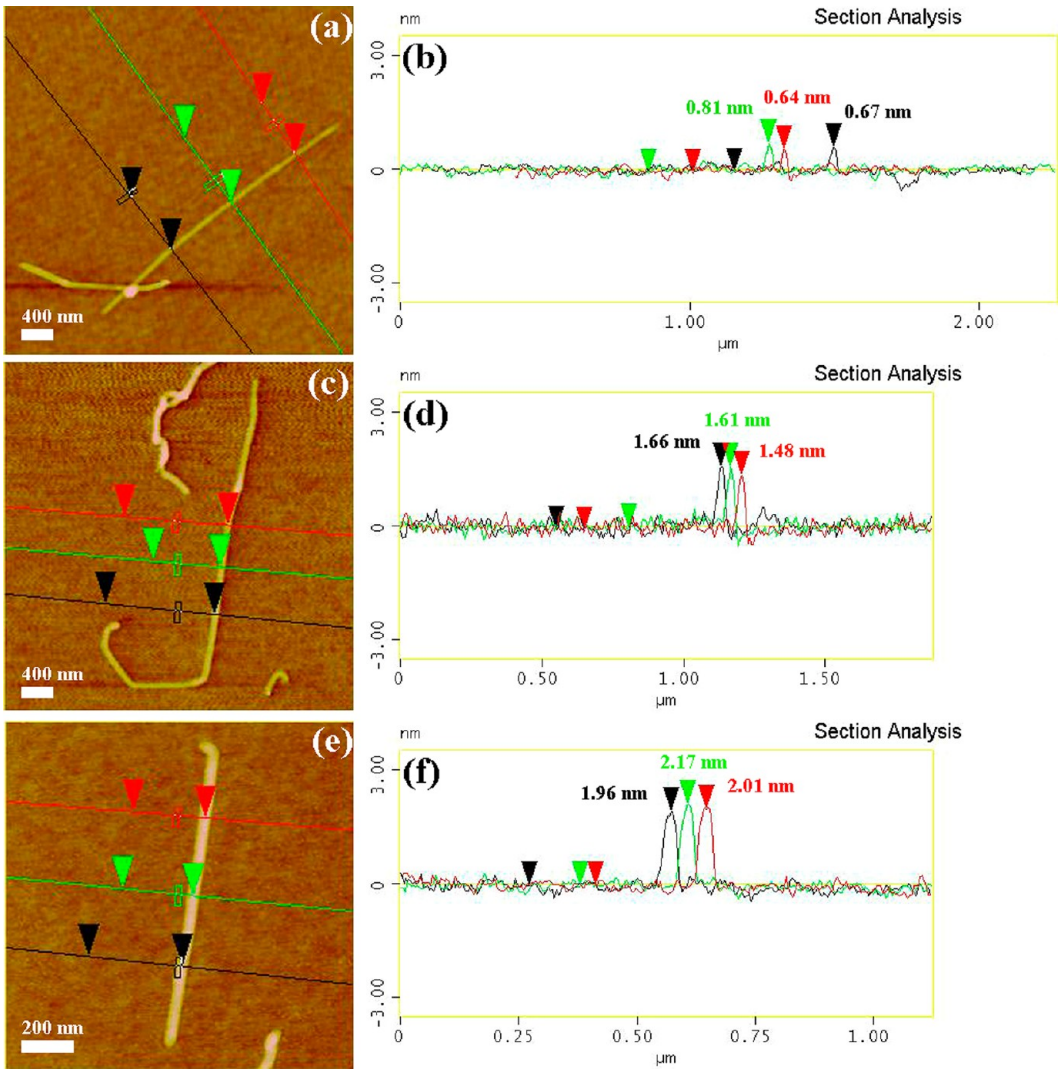


**Figure 3. AFM height measurements of the collapsed nanotubes. AFM images of collapsed (a) SWCNTs, (c) DWCNTs, and (e) TWCNTs. Ribbon-like structures are shown in AFM images. Height profiles of the corresponding collapsed (b) SWCNTs, (d) DWCNTs, and (f) TWCNTs. Height measurements were taken along the corresponding colored lines indicated in the AFM images.**

The heights were measured along the corresponding lines marked at three different set points along the nanotube length. The lengths of collapsed nanotubes in these images are typically 1−2.5 $\mu$m, much shorter than the CNT carpet height, probably due to cutting off during the sonication process. As shown in Figure 3b, the heights in three different regions are 0.6, 0.8, and 0.7 nm, corresponding to two closely stacked graphene layers. Height averaging along the length of the nanotube with a SIMAGIS software package (Carbon Nanotube Length, Height, Curvature, and Aspect Ratio Analysis. Ver. 2. Nanotechnology. Smart Imaging Technologies, Houston, Texas) provides an average height of 0.7 nm (more detailed information on measuring average height of nanotube by SIMAGIS can be found in Figure S4 and Table S1). This strongly indicates that the SWCNT has fully collapsed into a closed-edged bilayer graphene nanoribbon. A collapsed DWCNT with a length of ~3 $\mu$m is shown in Figure 3c, and the deformed parts that change the orientations of the nanotube are visible. The AFM section analysis shows the height of the nanotube is in the range of 1.4 to 1.7 nm, and a SIMAGIS average measurement gives an average height of ~1.3 nm, consistent with the height of a flattened DWCNT. When measuring a collapsed TWCNT, the AFM section analysis and a SIMAGIS measurement give an average height of 2.1 nm, which is consistent with the height of a fully collapsed TWCNT. The contrast variation shown in each AFM height image (Figure 3a,c,e) is also consistent, indicating the additional carbon layers in the collapsed DWCNTs and TWCNTs.

According to the structural identifiers for distinguishing the two different structures, we collected the total counts of collapsed and uncollapsed SWCNTs and DWCNTs from hundreds of HRTEM images. Coexistence of collapsed and uncollapsed structures can usually be found in one image. Sum counts of 641

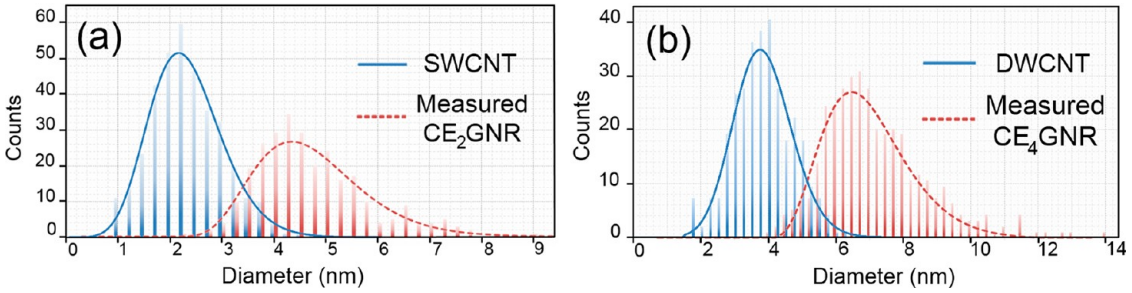


**Figure 4. (a) Size distribution of uncollapsed SWCNTs (diameters) and collapsed SWCNTs ($CE_2GNR$). (b) Size distribution of uncollapsed DWCNTs (diameters) and collapsed DWCNTs ($CE_4GNR$). Column bars showing that the counts *versus* diameters of each structure are fitted by the corresponding colored curves (blue and solid line for the uncollapsed structures, red and dashed line for the collapsed structures).**

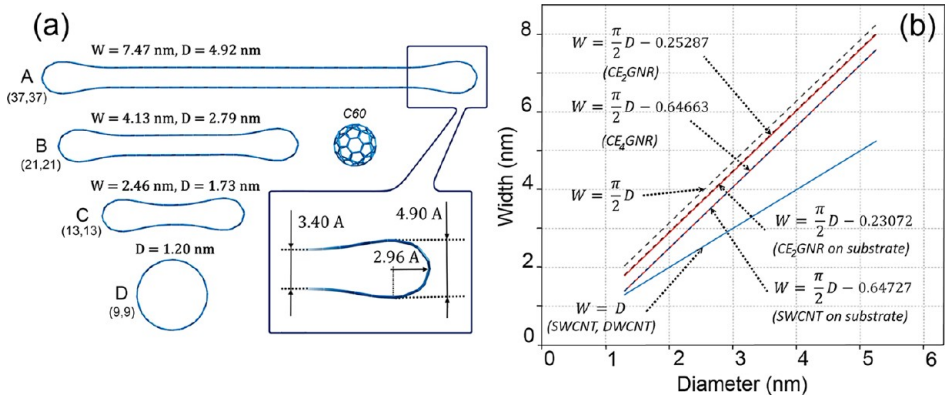


**Figure 5. (a) Uncollapsed and collapsed SWCNTs with different diameters in free space generated by LAMMPS molecular dynamics simulation. The geometry of a collapsed SWCNT consists of two highly strained bulbs on the two edges and a collapsed region where the two opposing walls are flattened and stabilized due to the van der Waals interaction, leaving the interlayer distance as 3.4 Å. The heights of the two-edged bulbs are found to be a constant around 4.9 Å, independent of initial diameter of the nanotube. The height of the bulb is comparable in size to $C_{60}$, as is shown in (a). (b) Linear relationships between measured width ($W$) and original cylindrical diameter ($D$) for uncollapsed and collapsed structures in free space (SWCNT, DWCNT, $CE_2GNR$, and $CE_4GNR$) and on a substrate (SWCNT on substrate and $CE_2GNR$ on substrate) are shown by the straight lines and their corresponding equations. For simple comparison, a conversion equation of $W = \pi D/2$ is given if the formation of highly strained bulbs is not taken into account.**

SWCNTs have been collected, in which the collapsed and uncollapsed SWCNTs account for 44 and 56%, respectively. Likewise, 650 DWCNTs have been counted, in which the collapsed and uncollapsed DWCNTs account for 53 and 47%, respectively. The fitting curves for the size distribution of the uncollapsed nanotubes (diameters of SWCNTs or DWCNTs) and the collapsed nanotubes (measured width of $CE_2GNR$ or $CE_4GNR$) are plotted in Figure 4.

In order to convert the widths of the collapsed SWCNTs and DWCNTs to the diameters of its uncollapsed state, we generated collapsed and uncollapsed SWCNTs with different diameters and optimized the geometry using molecular dynamics simulations implemented in LAMMPS (Figure 5). The van der Waals interaction energy reaches a maximum when the distance of two opposing walls gets close to 0.34 nm (as shown in the inset in Figure 5a), which is the interlayer spacing of adjacent sheets in a graphite crystal. The height of the highly strained bulbs on the two edges is found to be a constant around 0.49 nm independent of the initial nanotube diameter (Figure 5a), which is comparable to the diameter of $C_{60}$ (0.7 nm).[49] Therefore, the width of the fully collapsed structure is linearly dependent on the width of the flattened region which is set by its diameter as a cylinder. Using optimized geometries, we found linear relationship between the width of collapsed form and diameter of cylindrical form of the free-standing SWCNTs (Figure 5b). The same procedure was performed for SWCNTs and DWCNTs on a substrate (as a model of a substrate, we used a graphene plane for simplicity).

Using those equations, the measured widths of collapsed SWCNTs and DWCNTs in Figure 1 were converted into the diameters in their uncollapsed state. Figure 6 shows the resulting distribution of diameters of collapsed and uncollapsed SWCNTs and DWCNTs and their sum. The cross section point of the fitting curves of uncollapsed and collapsed structures is taken to represent the equivalent energy point (referred to as $D_{eqe}^{exp}$), at which there is no energy difference between the collapsed and uncollapsed nanotube. Below $D_{eqe}^{exp}$, the cylindrical tube is the

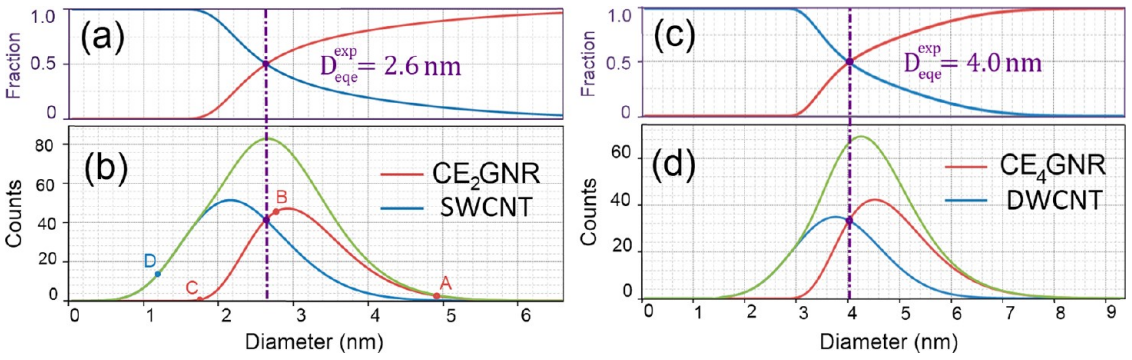


**Figure 6. Fraction of uncollapsed and collapsed SWCNTs (a) and DWCNTs (c) *versus* diameters in the sum. (b,d) Resulting diameter distributions of uncollapsed (SWNTs and DWNTs shown by blue fitting curves) and collapsed structures ($CE_2GNR$ and $CE_4GNR$ shown by red fitting curves) and their sum (shown by green fitting curves) after conversion of measured widths of the collapsed structures into the cylindrical diameters using the equations for $CE_2GNR$ and $CE_4GNR$ shown in Figure 5b. Cross section point of the fitting curves for uncollapsed and collapsed structure corresponds to the critical diameter ($D_{eqe}^{exp}$) ("exp" represents that the diameter is obtained from experimental data, "eqe" represents the equivalent energy point), above which the collapsed form of SWCNT or DWCNT is energetically favorable. From the fitting of our experimental data, the $D_{eqe}^{exp}$ values for SWCNTs and DWCNTs are found to be 2.6 and 4.0 nm, respectively.**

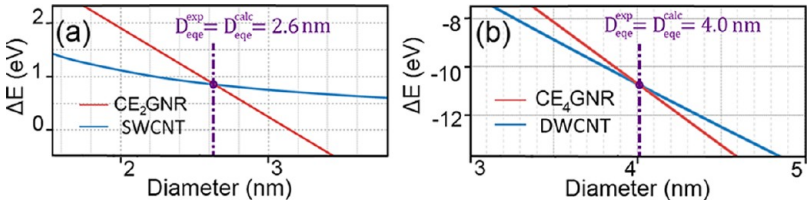


**Figure 7. Calculated energy for uncollapsed and collapsed SWCNTs (a) and DWCNTs (b) with different diameters in free space by performing LAMMPS molecular dynamics with AIREBO potential (no torsion term). The energies of uncollapsed SWCNTs and DWCNTs are shown by blue curves, and the energies of collapsed SWCNTs and DWCNTs are shown by red curves. By using van der Waals interaction energy $\varepsilon$ = 53.6 meV/pair, the calculated diameter $D_{eqe}^{cal}$ ("cal" represents the diameter that is obtained from calculation, "eqe" represents the equivalent energy point) corresponds very well to the $D_{eqe}^{exp}$ for both SWCNTs and DWCNTs.**

energetically favorable geometry, whereas the collapsed structure becomes energetically more stable when the diameter is above $D_{eqe}^{exp}$ because the van der Waals force between two walls will exceed bond bending stiffness. The $D_{eqe}^{exp}$ values for SWCNTs and DWCNTs are found to be 2.6 and 4.0 nm, respectively, from our experimental fitting. This determination of equal energies for the two structures assumes that they are in thermodynamic equilibrium with each other. It is also likely that the equilibrium temperature is close to the growth temperature, 750 °C, with the respective structure populations frozen by the rapid cooling of the sample. It is possible that the measured equivalent energy point is affected by the experimental miscounting of uncollapsed nanotubes since a collapsed tube can appear straight in TEM images. A sensitivity check of the energy equivalence point to miscounting was carried out by assuming that miscount of nanotubes may have occurred for nanotubes greater than 1.5 nm with the miscount increasing linearly by diameter up to 50% at a diameter of 6 nm. For this degree of miscounting, the energy equivalence point was found to decrease by only 0.1 nm. Calculations for different miscounts are shown in Figure S5. The structures corresponding to the diameters shown by A, B, C, and D in Figure 6a can be found in Figure 5a. Larger critical diameter for DWCNTs than that for SWCNTs can be interpreted from an energy point of view. Upon collapsing, the graphitic layers will increase their bending energy by forming the two-edged highly strained bulbs at the expense of the attractive van der Waals energy obtained by the innermost walls. The increase of the deformation energy from forming bulbs happens to each graphitic layer, whereas only the innermost walls gain the attractive energy. Therefore, the compensation to the increase of the deformation energy requires the increase of the $D_{eqe}$ with increasing the number of walls.[9,15] The fractions of the uncollapsed and collapsed SWCNTs and DWCNTs *versus* their diameters are shown on the top in Figure 6a,c, from which we can tell the population changing of the uncollapsed and collapsed structures below and above the $D_{eqe}^{exp}$. Moreover, given a certain diameter, the fraction of each structure as part of the sum is shown.

Using molecular dynamics with AIREBO potential (torsion term excluded to gain reasonable bending modulus of $k$ = 1.4 eV), we performed energy calculations for collapsed and uncollapsed tubes of different diameters, as shown in Figure 7. The energy of van der Waals interaction can be adjusted (in our simulations, it

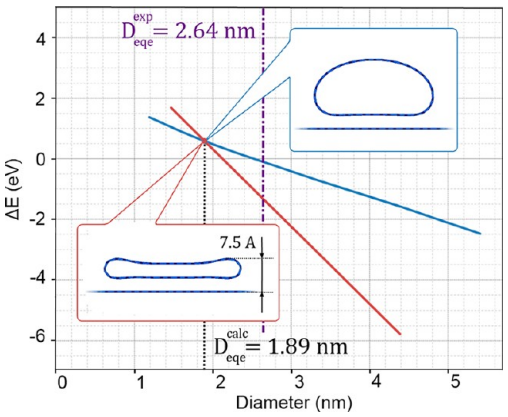


**Figure 8. Calculated energy for uncollapsed and collapsed SWCNTs on a single-layer graphene substrate. $D^{cal}_{eqe}$ of SWCNTs on a substrate is around 1.89 nm, smaller than the $D^{exp}_{eqe}$ of SWCNTs in free space. Energies of uncollapsed and collapsed SWCNTs on a substrate *versus* diameters are shown by blue and red lines, respectively. Correspondingly, their uncollapsed and collapsed geometries are also shown next to the energy curve.**

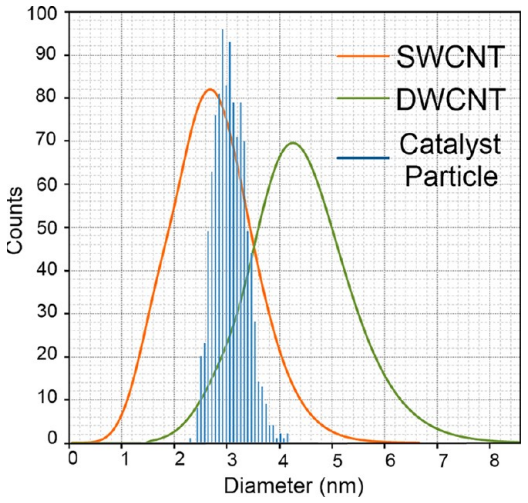


**Figure 9. Size distributions of the catalyst particles, sum of the SWCNTs, and sum of the DWCNTs. Size distribution of iron only catalyst particles (Fe) is obtained from that of the metal oxide particles ($AlFe_2O_4$) shown in the inset of Figure 1a.**

was represented by depth of minima of Lennard-Jones potential) in order to match $D^{cal}_{eqe}$ with $D^{exp}_{eqe}$. It was found that the value of $\varepsilon_{vdW}$ = 54 meV/pair is the best to achieve this goal. For DWCNTs, we used the same parameters as for SWCNTs and obtained good agreement with experimental data. The calculated energy changing of uncollapsed and collapsed structure around the equivalent energy point is consistent with other studies.[11,12,17]

Energy calculations are also performed for the SWCNT on a single-layer graphene substrate. The $D^{cal}_{eqe}$ for it was found to be 1.9 nm, smaller than that of the SWCNT in free space, which suggests that the substrate enhances the stability of the collapsed structure, consistent with the literature.[48] As shown in the upper geometry in Figure 8, the van der Waals interaction between the cylindrical SWCNT and substrate can distort its circular shape and induce a radial deformation. On the other hand, the rigid circular shape still tends to be maintained to the maximum extent at smaller tube diameters. The interplay between the surface van der Waals interaction and the rigid bond bending stiffness results in a partial collapsed and elliptical geometry.[13] The heights of the edged bulbs of the fully flattened SWCNT on a substrate are found to be 0.75 nm from the substrate surface, which is about twice the height of a single-layer graphene on substrate.

Figure 9 shows the diameter distributions of SWCNTs, DWCNTs, and catalyst particles. The particles playing the catalytic role in growing nanotubes are iron particles reduced from the metal oxide state. Their size distribution is calculated for the iron only size from the metal oxide particle size distribution and percent of iron in the oxide and the density of Fe (7.8 g/mL) and $AlFe_2O_4$ (4.6 g/mL). Compared to the initial monodisperse nanoparticles, the broadened size distribution of the SWCNTs and DWCNTs is a strong indication that Ostwald ripening, where some particles grow larger and some smaller, takes place during the preheating, reduction, and growth process. Also, clearly, the growth of double-walled nanotubes is strongly favored at larger diameters.

## CONCLUSIONS

In summary, large-diameter few-walled carbon nanotubes (CNTs) have been produced using nearly monodispersed preformed aluminum ferrite nanoparticles with an average diameter of 4.0 ± 0.4 nm. CNTs with sufficiently large diameter are observed to collapse into closed-edged graphene nanoribbons ($CE_xGNR$), including collapsed SWCNTs, DWCNTs, and TWCNTs. TEM characterization of $CE_xGNR$ shows collapsed *versus* uncollapsed in the presence of kinked, folded, or twisted deformations as an indicator that a carbon nanotube has collapsed into a ribbon-like structure, while uncollapsed are identified by a lack of such structures and are typically observed to be straight. Using the structural identifiers, diameters and measured widths of abundant collapsed and uncollapsed SWCNTs and DWCNTs have been collected from TEM images. By experimentally fitting the size distribution and computationally calculating the energy of the uncollapsed and collapsed SWCNTs and DWCNTs, a zero energy difference between the two forms for SWCNTs and DWCNTs is found at 2.6 and 4.0 nm, respectively, with the assumption equilibrium between the two states. Theory also indicates that the $D_{eqe}$ is even smaller for tubes sitting on a surface (*i.e.*, 1.9 nm for a SWCNT sitting on a graphene surface). The assignment of

equal energy for the two structures at a diameter where the populations of both are equal makes the assumption that the two structures are in thermodynamic equilibrium at a temperature that is likely to be near the growth temperature of 750 °C since the sample is rapidly cooled to room temperature from the growth temperature. This also assumes that the population change of the uncollapsed and collapsed SWCNTs and DWCNTs around the equal energy diameter provides a measure of the fraction of each structure for specific diameters at the growth temperature.

Of significant interest is that collapsed nanotubes provide a route to well-defined two, four, *etc*. layered graphene nanoribbons with a well-defined edge. It is of great interest and a considerable challenge to further experimentally characterize the $CE_x$GNTs electrically and optically and determine whether the original chirality of a uncollapsed tube influences the properties of the collapsed graphene nanoribbon. Because the edges are highly strained it is also likely that one can selectively functionalize the edges to further effect interesting electrical and optical changes.

## METHODS

**Chemicals.** Iron oxide, hydrated FeO(OH) (catalyst grade, 30−50 mesh), oleic acid (technical grade, 90%), and 1-octadecene (ODE, technical grade, 90%) were purchased from Sigma-Aldrich. Iron oleate ([Fe] = 3 mg/mL) was synthesized using the method mentioned in the previous research,[50] and aluminum oleate was purchased by Fisher Scientific. All iron oxide nanoparticles were synthesized under nitrogen. Aluminum iron oxide was obtained by modifying the standard method for monodispersed iron oxide nanocrystals; iron and aluminum oleate were decomposed in the presence of oleic acid at 320 °C for 2 h.[50] For the purification of as-synthesized nanocrystals, 5 mL of resulting colloid was washed and precipitated using 25 mL of methanol and 25 mL of acetone by centrifugation at 4500 rpm for 30 min. The resulting black colloid was redispersed in 15 mL of hexane.

**Synthesis of Catalyst and Large-Diameter CNTs.** The following synthetic process involving deposition of catalyst particles on a substrate and growth of collapsed CNTs is illustrated in Figure 1a. The substrate was prepared using a $SiO_2$ wafer, on which the $Al_2O_3$ layer was formed by sputtering aluminum or spin coating water-dispersed alumoxane solution. An aluminum layer with a uniform thickness of 10 nm was prepared in a sputter coater. Synthesis of water-soluble $Al_2O_3$ particles and fabrication of an $Al_2O_3/SiO_2$ layer from solution were achieved by a previously reported technique.[51] A preformed $AlFe_2O_4$ nanoparticle solution was diluted into different concentrations, followed by drop drying onto $Al_2O_3/SiO_2$ substrates. Prior to growth, in order to remove the oleic acid coating and expose the preformed metal oxide nanoparticles, the samples were calcined at 200 °C for 2 h in oxygen with a flow rate of 200 sccm. The growth of carbon nanotubes was carried out in a hot filament chemical vapor deposition (CVD) apparatus at 750 °C, which has been described elsewhere.[43,52] $H_2$ (210 sccm) and $C_2H_2$ (2 sccm) were supplied during the reduction and growth stages as reducing agent and carbon source gas, respectively. $H_2O$ was supplied by bubbling $H_2$ throughout degassed water at 200 sccm to assist carpet supergrowth. The catalyst particles were reduced at 25 Torr in a 30 s reduction process, during which a tungsten filament was activated by ramping to a current of 9−10 A. The high temperature of the filament (typically ∼2500 °C) enables dissociation of $H_2$ to form atomic hydrogen, which rapidly reduced the preformed nanoparticles to catalytically active metal particles. The pressure was then reduced to approximately 4 Torr, and the hot filament was switched off. Nanotube growth was then continued for an additional 10 min.

*Conflict of Interest:* The authors declare no competing financial interest.

*Acknowledgment.* The authors thank M. Nguyen for aiding characterizations by AFM, Y. Zhu for helpful discussions, S. Ripley for assistance and maintenance of the hot-filament reactor, Prof. N. Zhao and Prof. J. Li at Tianjin University for helpful discussion and assistance, and the China Scholarship Council for partial support this research. This research was funded by Lockheed Martin, NSF EEC-0647452 and UTA/AEC BEG08-011, and the ONR MURI Program (#00006766, N00014-09-1-1066) and the Air Force Research Laboratory under agreement number FA8650-07-2-5061.

*Supporting Information Available:* TEM, AFM images, and XRD pattern of the nearly monodispersed preformed $AlFe_2O_4$ nanoparticles with an average diameter of 4.0 ± 0.4 nm. Pictures showing the bottom G/D ratio, top G/D ratio, and height of nanotube carpet grown from preformed $AlFe_2O_4$ nanoparticles *versus* the nanoparticle concentration. More HRTEM images of the collapsed SWCNTs with bended, kinked, and flattened features in their structures. Nanotube height averaging along the length measured by a SIMAGIS software package. Table of detailed information in the height measurements of the collapsed structures ($CE_2$GNR, $CE_4$GNR, and $CE_6$GNR) provided by SIMAGIS software package. This material is available free of charge *via* the Internet at http://pubs.acs.org.

## REFERENCES AND NOTES

1. Javey, A.; Shim, M.; Dai, H. J. Electrical Properties and Devices of Large-Diameter Single-Walled Carbon Nanotubes. *Appl. Phys. Lett.* **2002**, *80*, 1064–1066.
2. Kurachi, H.; Uemura, S.; Yotani, J.; Nagasako, T.; Yamada, H.; Ezaki, H.; Maesoba, T.; Loutfy, R.; Moravsky, A.; Nakazawa, T.; *et al.* FED with Double-Walled Carbon Nanotube Emitters. *Proceedings of 21st International Display Research Conference/8th International Display Workshops*; Society for Information Display: San Jose, CA, 2001; pp 1237−1240.
3. Dillon, A. C.; Jones, K. M.; Bekkedahl, T. A.; Kiang, C. H.; Bethune, D. S.; Heben, M. J. Storage of Hydrogen in Single-Walled Carbon Nanotubes. *Nature* **1997**, *386*, 377.
4. Lebedkin, S.; Schweiss, P.; Renker, B.; Malik, S.; Hennrich, F.; Neumaier, M.; Stoermer, C.; Kappes, M. M. Single-Wall Carbon Nanotubes with Diameters Approaching 6 nm Obtained by Laser Vaporization. *Carbon* **2002**, *40*, 417–423.
5. Kiang, C. H. Growth of Large-Diameter Single-Walled Carbon Nanotubes. *J. Phys. Chem. A* **2000**, *104*, 2454–2456.
6. Yang, Q. H.; Bai, S.; Sauvajol, J. L.; Bai, J. B. Large-Diameter Single-Wall Carbon Nanotubes Synthesized by Chemical Vapor Deposition. *Adv. Mater.* **2003**, *15*, 792–795.
7. Cheung, C. L.; Kurtz, A.; Park, H.; Lieber, C. M. Diameter-Controlled Synthesis of Carbon Nanotubes. *J. Phys. Chem. B* **2002**, *106*, 2429–2433.
8. Zhou, W. W.; Ding, L.; Yang, S. W.; Liu, J. Synthesis of High-Density, Large-Diameter, and Aligned Single-Walled Carbon Nanotubes by Multiple-cycle Growth Methods. *ACS Nano* **2011**, *5*, 3849–3857.
9. Chopra, N. G.; Benedict, L. X.; Crespi, V. H.; Cohen, M. L.; Louie, S. G.; Zettle, A. Fully Collapsed Carbon Nanotubes. *Nature* **1995**, *377*, 135–138.

10. Benedict, L. X.; Chopra, N. G.; Cohen, M. L.; Zettl, A.; Louie, S. G.; Crespi, V. H. Microscopic Determination of the Interlayer Binding Energy in Graphite. *Chem. Phys. Lett.* **1998**, *286*, 490–496.
11. Gao, G. H.; Cagin, T.; Goddard, W. A. Energetics, Structure, Mechanical and Vibrational Properties of Single-Wall Carbon Nanotubes. *Nanotechnology* **1998**, *9*, 184–191.
12. Liu, H. J.; Cho, K. J. A Molecular Dynamics Study of Round and Flattened Carbon Nanotube Structures. *Appl. Phys. Lett.* **2004**, *85*, 807–809.
13. Elliott, J. A.; Sandler, J. K. W.; Windle, A. H.; Young, R. J.; Shaffer, M. S. P. Collapse of Single-Wall Carbon Nanotube Is Diameter Dependent. *Phys. Rev. Lett.* **2004**, *92*, 095501(1−5).
14. Liu, B.; Yu, M. F.; Huang, Y. G. Role of Lattice Registry in the Full Collapse and Twist Formation of Carbon Nanotubes. *Phys. Rev. B* **2004**, *70*, 161402(R).
15. Xiao, J.; Liu, B.; Huang, Y.; Zuo, J.; Hwang, K. C.; Yu, M. F. Collapse and Stability of Single- and Multi-Wall Carbon Nanotubes. *Nanotechnology* **2007**, *18*, 395703(1−7).
16. Tang, T.; Jagota, A.; Hui, C. Y.; Glassmaker, N. J. Collapse of Single-Wall Carbon Nanotubes. *J. Appl. Phys.* **2005**, *97*, 074310.
17. Zhang, S. L.; Khare, R.; Belytschko, T.; Hsia, K. J.; Mielke, S. L.; Schatz, G. C. Transition States and Minimum Energy Pathways for the Collapse of Carbon Nanotubes. *Phys. Rev. B* **2006**, *73*, 075423.
18. Pantano, A.; Parks, D. M.; Boyce, M. C. Mechanics of Deformation of Single- and Multi-Wall Carbon Nanotubes. *J. Mech. Phys. Solids* **2004**, *52*, 789–821.
19. Chang, T. C.; Guo, Z. R. Temperature-Induced Reversible Dominoes in Carbon Nanotubes. *Nano Lett.* **2010**, *10*, 3490–3493.
20. Sun, D. Y.; Shu, D. J.; Ji, M.; Liu, F.; Wang, M.; Gong, X. G. Pressure-Induced Hard-to-Soft Transition of a Single Carbon Nanotube. *Phys. Rev. B* **2004**, *70*, 165417.
21. Zhang, X. H.; Sun, D. Y.; Liu, Z. F.; Gong, X. G. Structure and Phase Transitions of Single-Wall Carbon Nanotube Bundles under Hydrostatic Pressure. *Phys. Rev. B* **2004**, *70*, 035422.
22. Wang, Z. W. Formation of a Quenchable Dense Carbon Form by Compression of Double-Walled Carbon Nanotubes. *J. Phys. Chem. B* **2004**, *108*, 18192–18194.
23. Hertel, T.; Walkup, R. E.; Avouris, P. Deformation of Carbon Nanotubes by Surface van der Waals Forces. *Phys. Rev. B* **1998**, *58*, 13870–13873.
24. Ruoff, R. S.; Tersoff, J.; Lorents, D. C.; Subramoney, S.; Chan, B. Radial Deformation of Carbon Nanotubes by van der Waals Forces. *Nature* **1993**, *364*, 514–516.
25. Qian, W. Z.; Wei, F.; Liu, T.; Wang, Z. W. What Causes the Carbon Nanotubes Collapse in a Chemical Vapor Deposition Process. *J. Chem. Phys.* **2003**, *118*, 878–882.
26. Yu, M. F.; Lourie, O.; Dyer, M. J.; Moloni, K.; Kelly, T. F.; Ruoff, R. S. Strength and Breaking Mechanism of Multi-Walled Carbon Nanotubes under Tensile Load. *Science* **2000**, *287*, 637–640.
27. Yakobson, B. I.; Campbell, M. P.; Brabec, C. J.; Bernholc, J. High Strain Rate Fracture and C-Chain Unraveling in Carbon Nanotubes. *Comput. Mater. Sci.* **1997**, *8*, 341–348.
28. Crespi, V. H.; Chopra, N. G.; Cohen, M. L.; Zettl, A.; Louie, S. G. Anisotropic Electron-Beam Damage and the Collapse of Carbon Nanotubes. *Phys. Rev. B* **1996**, *54*, 5927–5931.
29. Chang, T. C. Dominoes in Carbon Nanotubes. *Phys. Rev. Lett.* **2008**, *101*, 177501.
30. Shklyaev, O. E.; Mockensturm, E.; Crespi, V. H. Modeling Electrostatically Induced Collapse Transitions in Carbon Nanotubes. *Phys. Rev. Lett.* **2011**, *106*, 155501.
31. Yakobson, B. I.; Brabec, C. J.; Bernholc, J. Structural Mechanics of Carbon Nanotubes: From Continuum Elasticity to Atomistic Fracture. *J. Comput.-Aided Mater. Des.* **1996**, *3*, 173–182.
32. Crespi, V. H.; Chopra, N. G.; Cohen, M. L.; Zettl, A. Site-Selective Radiation Damage of Collapsed Carbon Nanotubes. *Appl. Phys. Lett.* **1998**, *73*, 2435–2437.
33. Martel, R.; Schmidt, T.; Shea, H. R.; Hertel, T.; Avouris, Ph. Single- and Multi-Wall Carbon Nanotube Field-Effect Transistors. *Appl. Phys. Lett.* **1998**, *73*, 2447–2449.
34. Lammert, P. E.; Zhang, P. H.; Crespi, V. H. Gapping by Squashing: Metal−Insulator and Insulator−Metal Transitions in Collapsed Carbon Nanotubes. *Phys. Rev. Lett.* **2000**, *84*, 2453–2455.
35. Giusca, C. E.; Tison, Y.; Silva, S. R. P. Atomic and Electronic Structure in Collapsed Carbon Nanotubes Evidenced by Scanning Tunneling Microscopy. *Phys. Rev. B* **2007**, *76*, 035429.
36. Yu, M. F.; Dyer, M. J.; Chen, J.; Qian, D.; Liu, W. K.; Ruoff, R. S. Locked Twist in Multiwalled Carbon-Nanotube Ribbons. *Phys. Rev. B* **2001**, *64*, 241403(R).
37. Bourgeois, L. N.; Bursill, L. A. High-Resolution Transmission Electron Microscopy and Energetics of Flattened Carbon Nanoshells. *Chem. Phys. Lett.* **1997**, *277*, 571–578.
38. Motta, M.; Moisala, A.; Kinloch, I. A.; Windle, A. H. High Performance Fibres from `Dog Bone' Carbon Nanotubes. *Adv. Mater.* **2007**, *19*, 3721–3726.
39. Yu, M. F.; Kowalewski, T.; Ruoff, R. S. Investigation of the Radial Deformability of Individual Carbon Nanotubes under Controlled Indentation Force. *Phys. Rev. Lett.* **2000**, *85*, 1456–1459.
40. Yu, M. F.; Kowalewski, T.; Ruoff, R. S. Structural Analysis of Collapsed, and Twisted and Collapsed, Multiwalled Carbon Nanotubes by Atomic Force Microscopy. *Phys. Rev. Lett.* **2001**, *86*, 87–90.
41. Kiang, C. H.; Goddard, W. A.; Beyers, R.; Bethune, D. S. Structural Modification of Single-Layer Carbon Nanotubes with an Electron Beam. *J. Phys. Chem.* **1996**, *100*, 3749–3752.
42. Ci, L. J.; Vajtai, R.; Ajayan, P. M. Vertically Aligned Large-Diameter Double-Walled Carbon Nanotube Arrays Having Ultralow Density. *J. Phys. Chem. C* **2007**, *111*, 9077–9080.
43. Alvarez, N. T.; Li, F.; Pint, C. L.; Mayo, J. T.; Fisher, E. Z.; Tour, J. M.; Colvin, V. L.; Hauge, R. H. Uniform Large Diameter Carbon Nanotubes in Vertical Arrays from Premade Near-Monodisperse Nanoparticles. *Chem. Mater.* **2011**, *23*, 3466–3475.
44. Kong, J.; Soh, H. T.; Cassell, A. M.; Quate, C. F.; Dai, H. J. Synthesis of Individual Single-Walled Carbon Nanotubes on Patterned Silicon Wafers. *Science* **1998**, *395*, 878–881.
45. Bernholc, J.; Brabec, C.; Buongiorno, N. M.; Maiti, A.; Roland, C.; Yakobson, B. I. Theory of Growth and Mechanical Properties of Nanotubes. *Appl. Phys. A: Mater. Sci. Process.* **1998**, *67*, 39–46.
46. Li, W. Z.; Yan, X.; Kempa, K.; Ren, Z. F.; Giersig, M. Structure of Flattened Carbon Nanotubes. *Carbon* **2007**, *45*, 2938–2945.
47. Liu, S. W.; Yue, J.; Wehmschulte, R. J. Large Thick Flattened Carbon Nanotubes. *Nano Lett.* **2002**, *2*, 1439–1442.
48. Yu, M. F.; Dyer, M. J.; Ruoff, R. S. Structure and Mechanical Flexibility of Carbon Nanotube Ribbons: An Atomic-Force Microscopy Study. *J. Appl. Phys.* **2001**, *89*, 4554–4557.
49. Kroto, H. W.; Heath, J. R.; O'Brien, S. C. O.; Curl, R. F.; Smalley, R. E. C60: Buckminsterfullerene. *Nature* **1985**, *318*, 162–163.
50. Yu, W. W.; Falkner, J. C.; Yavuz, C. T.; Colvin, V. L. Synthesis of Monodisperse Iron Oxide Nanocrystals by Thermal Decomposition of Iron Carboxylate Salts. *Chem. Commun.* **2004**, 2306–2307.
51. Alvarez, N. T.; Hamilton, C. E.; Pint, C. L.; Orbaek, A.; Yao, J.; Frosinini, A.; Barron, A.; Tour, J. M.; Hauge, R. H. Wet Catalyst-Support Films for Production of Vertically Aligned Carbon Nanotubes. *ACS Appl. Mater. Interfaces* **2010**, *2*, 1851–1856.
52. Pint, C. L.; Pheasant, S. T.; Parra-Vasquez, N. G.; Horton, C.; Xu, Y. Q.; Hauge, R. H. Investigation of Optimal Parameters for Oxide-Assisted Growth of Vertically Aligned Single-Walled Carbon Nanotubes. *J. Phys. Chem. C* **2009**, *113*, 4125–4133.